15

# Denoising of Fluorescence Confocal Microscopy Images with Photobleaching compensation in a Bayesian framework

Isabel Rodrigues[1,3] and João Sanches[2]
*Institute for Systems and Robotics[1], Instituto Superior Técnico[2],*
*Instituto Superior de Engenharia de Lisboa[3]*
*Portugal*

## 1. Introduction

Fluorescence confocal microscopy imaging is today one of the most important tools in biomedical research. In this modality the image intensity information is obtained from specific tagging proteins that fluoresce nanoseconds after the absorption of photons associated with a specific wavelength radiation. Additionally, the confocal technology rejects all the out-focus radiation, thereby allowing 3-D imaging almost without blur. Therefore, this technique is highly selective allowing the tracking of specific molecules, tagged with fluorescent dye, in living cells (J.W.Lichtman & J.A.Conchello, 2005). However, several difficulties associated with this technology such as multiplicative noise, *photobleaching* and photo-toxicity, affect the observed images. These undesirable effects become more serious when higher acquisition rates are needed to observe fast kinetic processes in living cells.

One of the main sources of these problems resides on the huge amount of amplification used to amplify the small amount of radiation captured by the microscope, required to observe the specimen. The amplification process, based on photo-multiplicative devices, generates images corrupted by a type of multiplicative noise with Poisson distribution, characteristic of low photon counting process (R. Willett, 2006). In fact the number of photons that are collected by the detector at each point in the image determines the signal quality at that point. The noise distorting these images is in general more limiting than the resolution of the confocal microscope.

The fluorophore is the component of the molecule responsible for its capability to fluoresce. The *photobleaching* effect consists on the irreversible destruction of the fluorescence of the fluorophores due to photochemical reactions induced by the incident radiation (J.Braga et al., 2004; Lippincott-Schwarz et al., 2003). Upon extended excitation all the fluorophores will eventually photobleach, which leads to a fading in the intensity of sequences of acquired images along the time. This effect prevents long exposure time experiments needed to analyse biologic processes with a long lasting kinetics (Lippincott-Schwarz et al., 2001).

The photochemical reactions associated with the *photobleaching* effect also produce free radicals toxic to the specimen. This photo-toxicity (J.W.Lichtman & J.A.Conchello, 2005) effect increases along with the power of the incident radiation.

Establishing the right amount of incident radiation is a key point in this microscope modality. On one hand, increasing the illumination increases the photon count which improves the quality of the signal, but on the other hand, this increasing of the incident radiation speeds up the *photobleaching* and photo-toxicity effects that increase the quality degradation of the acquired images and in the limit, may lead to a premature death of the cells.

Many algorithms that deal with this type of microscopy images are conceived under the assumption of the *additive white Gaussian noise* (AWGN) model. However, the *multiplicative white Poisson noise* (MWPN) model is more appropriated to describe the noise corrupting laser scanning fluorescence confocal microscope (LSFCM) images due to the photon-limited characteristics, whose main attribute is its dependence on the image intensity. In order to take advantage of all the knowledge on AWGN denoising, some authors, instead of using the Poisson statistics of the noisy observations, they prefer to modify it introducing variance stabilizing transformations, such as the Anscombe or the Fisz transforms (M.Fisz,1955; P.Fryźlewicz & G.Nason, 2001). However, even applying the Anscombe transform, the additive AWGN assumption is accurate only when each photon count is larger than thirty (R.Willett, 2006).

In the seventies, W.H. Richardson and L. Lucy in separate works developed a specific methodology for data following a Poisson distribution. The Richardson-Lucy (R-L) algorithm can be viewed as an Expectation-Maximization (EM) algorithm including a Poisson statistical noise model. This algorithm presents several weaknesses such as the amplification of the noise after a few iterations, in particular when the *signal to noise ratio* (SNR) is low, which is the case of LSFCM images.

More recently several works on denoising methods applied to photon-limited imaging have come up in the literature. Methods based on wavelet and other similar transforms were developed by several authors (K. Timmermann & R. Nowak, 1999), (P.Besbeas et al., 2004), (R.Willett & R. Nowak, 2004), among many others. In conjunction with the use of the Poisson statistics, in the Bayesian framework, several regularization schemes have been proposed. Dey et al. from INRIA have proposed diverse deconvolution/denoising methods in the Bayesian framework for confocal microscopy with *total variation* (TV) regularization (N. Dey et. al. 2004, 2006). The authors conceived a combination of the R-L algorithm with a regularizing TV based constraint, whose smoothing avoids oscillations in homogeneous regions while preserving edges. The TV regularization was also used in conjunction with a multilevel algorithm for Poisson noise removal (Chan & Chen, 2007). Adaptive window approaches have been conceived for Poisson noise reduction and morphology preserving in Confocal Microscopy (C.Kervrann & A.Trubuil, 2004). Non-parametric regression methods have been developed in (J.Boulanger et al., 2008) for the denoising of sequences of fluorescence microscopy volumetric images (3-D+t). In this case the authors adopted a variance stabilizing procedure with a generalized Ascombe transform to combine Poisson and Gaussian noise models and proposed an adaptive patch-based framework able to preserve space-time discontinuities and simultaneously to reduce the noise level of the sequences. Other approach was proposed by Dupé (Dupé, et al., 2008) where a deconvolution algorithm uses a fast proximal backward-forward spitting iteration which

minimizes an energy function whose data fidelity term accounts for Poisson noise and an $L_1$ non-smooth sparsity regularization term acts upon the coefficients of a dictionary of transforms such as wavelets and curvelets.

Here a denoising algorithm for Poisson data that explicitly takes into account the *photobleaching* effect is presented, under the assumption that among all the complex mechanisms associated to overlapping phenomena that can cause the fading of the intensity in fluorescence microscopy, the photochemical one is the most relevant.

The main goal of the proposed algorithm is to estimate the time and space varying morphology of the cell nucleus and simultaneously the intensity decay rate due to *photobleaching* of fluorescence microscopy images of human cells.

The intensity decrease along the time is modelled by a decaying exponential with a constant rate. The algorithm is formulated in the Bayesian framework as an optimization task where a convex energy function is minimized.
*Maximum a posteriori* (MAP) estimation criterion is employed since it has been successfully used in other modalities, specially for image restoration purposes.
In general the denoising process is an ill-posed and an ill-conditioned problem (Vogel, 1998) requiring some sort of regularization. In the Bayesian framework the regularization effect is achieved by using *a prior* distribution functions that are jointly maximized with the distribution functions associated with the observation model describing the noise generation process.
Given the characteristics of these images, the local markovianity of the nucleus morphology seams to be a reasonable assumption. Thus, according to the Hammersley-Clifford theorem (J.Besag, 1986), a Gibbs distribution with appropriate potentials can be considered as the ***a prior*** knowledge about the cell nucleus morphology.
Several potentials have been proposed in the literature (T.Hebert & R.Leahy, 1989) and among them, one of the most popular of these functions is the quadratic, mainly for the sake of mathematic simplicity. However this function over-smoothes the solution. Since it is assumed that the morphology of the cell consists of sets of homogeneous regions separated by well defined boundaries, an alternative is the use of *edge preserving priors* such as *total variation* (TV) based potential functions that have been applied with success in several problems (L. I. Rudin et al., 1992; J. Bardsley & A. Luttman, 2006; N. Dey et al., 2004).
Very recently a new type of norms, called log-*Euclidean* norms, was proposed in (V. Arsigny et al., 2006). The interaction between neighbouring pixels that regularizes the solution imposed by the potential functions using this type of norms is based on the ratio of their intensities and not on its difference. This new approach is particularly suitable to be used in this case due to the positive nature of the optimization task associated with the denoising process of the LSFCM images. The advantage of this type of norms is more perceivable in small intensity regions where differences between neighbours are small while their ratios may exhibit relevant values. The penalization cost obtained with difference based priors may not be enough to remove the noise in these small intensity regions while the penalization costs induced by the ratio based priors may be strong enough to do it.

In this paper these log-Euclidean norms are jointly used with the total variation based priors to improve the performance of the denoising algorithm in the small intensity regions and simultaneously preserve the transitions across the entire image due to the TV approach.
Synthetic data were generated with a low level of SNR and Monte Carlo experiments were carried on with these data in order to evaluate the performance of the algorithm.
Real data of a HeLa immortal cell nucleus (D.Jackson, 1998), acquired by a laser scanning fluorescence confocal microscope (LSFCM), are used to illustrate the application of the algorithm.

## 2. Problem Formulation

Each sequence of $M \times N$ fluorescence microscopy images under analysis, $Y$, corresponds to L observations of a cell nucleus acquired along the time. Data can be represented by a 3D tensor, $Y = \{y_{i,j,t}\}$, with $0 \le i, j, t \le N-1, M-1, L-1$. Each pixel, $y_{i,j,t}$, is corrupted by Poisson noise and the time intensity decrease due to the *photobleaching* effect is modelled by a decaying exponential whose rate, denoted by λ, is assumed to be constant in time and in space.
The goal of the algorithm described here is the estimation of human cells morphology along the time as well as the intensity decay rate, λ, associated with the *photobleaching* effect, from the noisy sequence $Y$, usually exhibiting a low *signal to noise* ratio (SNR).

The proposed method consists of an iterative algorithm performed in two-steps. In the first step the intensity decay rate coefficient, λ, is estimated jointly with a crude time invariant basic morphology version of the cell.
In the second step a more realistic time and space varying version of the cell nucleus morphology is estimated by using the intensity decay rate coefficient, λ, obtained in the previous step.
The overall estimation process needs to be decomposed in these two steps in order to decouple the sources of intensity changes which are the *photobleaching* effect, estimated in the first step, and the real cell morphology changes in time and space, estimated in the second step.

### 2.1 Step one

Let us focus now on the first step of the algorithm where the rate of decay due to the *photobleaching* is estimated.
Let X be an approximated noiseless version of the noisy data, $Y$, where

$$x_{i,j,t} = g_{i,j}\ e^{-\lambda t} \tag{1}$$

$\mathbf{G} = \{g_{i,j}\}$, with $0 \le i, j \le N-1, M-1$, represents a time invariant version of the cell morphology and $e^{-\lambda t}$ represents the time intensity decay term that models the *photobleaching* effect. By adopting this model all the time variability of the intensity in the images is caught by the exponential term in order to accurately estimate the rate of decay due to the *photobleaching*.

A Bayesian approach using the *maximum a posteriori* (MAP) criterion is adopted to estimate **G** and λ. The problem may be formulated as the following energy optimization task

$$\left(\hat{\mathbf{G}},\hat{\lambda}\right)=\underset{\mathbf{G},\lambda}{\operatorname{argmin}}\ \mathbf{E}\left(\mathbf{G},\lambda,\mathbf{Y}\right) \tag{2}$$

where the energy function $\mathbf{E}(\mathbf{G},\lambda,\mathbf{Y})=\mathbf{E}_{\mathbf{Y}}(\mathbf{G},\lambda,\mathbf{Y})+\mathbf{E}_{\mathbf{G}}(\mathbf{G})$ is the sum of two terms, a data fidelity term, $\mathbf{E}_{\mathbf{Y}}(\mathbf{G},\lambda,\mathbf{Y})$, and a prior term, $\mathbf{E}_{\mathbf{G}}(\mathbf{G})$, needed do regularize the solution. The *a priori* information for λ is merely its overall constancy. The first term of this sum pushes the solution towards the observations according to the type of noise corrupting the images and the *a priori* energy term penalizes the solution in agreement with some previous knowledge about **G** (T. K. Moon & W. C. Stirling, 2000).

Assuming the independence of the observations the *data fidelity term*, which is the anti-logarithm of the *likelihood* function, is

$$\mathbf{E}_{\mathbf{Y}}(\mathbf{G},\lambda,\mathbf{Y})=-\log\left[\prod_{i,j,t=0}^{N-1,M-1,L-1}p\left(y_{i,j,t}\,|\,g_{i,j},\lambda\right)\right] \tag{3}$$

where $p\left(y_{i,j,t}\,|\,g_{i,j},\lambda\right)=\dfrac{\left(g_{i,j}e^{-\lambda t}\right)^{y_{i,j,t}}}{y_{i,j,t}!}e^{-g_{i,j}e^{-\lambda t}}$ is the Poisson distribution, yielding

$$\mathbf{E}_{\mathbf{Y}}(\mathbf{G},\lambda,\mathbf{Y})=\sum_{i,j,t}\left[g_{i,j}e^{-\lambda t}-y_{i,j,t}\log\left(g_{i,j}e^{-\lambda t}\right)\right]+C \tag{4}$$

The prior term regularizes the solution and helps to remove the noise. By assuming **G** as a *Markov random field* (MRF), p(**G**) can be written as a Gibbs distribution, $p(\mathbf{G})=\dfrac{1}{Z}e^{-\sum_{c\in C}V(g_c)}$, where *Z* is the partition function and $V(.)$ are the *clique potentials* (S.Geman & D.Geman, 1984). The sum of all *clique potentials*, the negative of the exponential argument function, is called the Gibbs energy, $\mathbf{E}_{\mathbf{G}}(\mathbf{G})$. In order to preserve the edges of the cell morphology *log-total variation* (log-TV) potentials are used in the regularization term. These potential functions have shown to be appropriated to deal with this type of optimization problems in $R_{+}^{N}$ (V. Arsigny et al., 2006).

The regularization based on quadratic potentials is often used because they simplify the mathematical formulation of the estimation problem. However, they over-smooth the solution, leading to significant loss of morphological details. On the contrary, the log-TV prior is more efficient to attenuate small differences among neighbouring nodes due to the noise, but it penalizes less the large amplitude differences due to the transitions. Additionally, this prior is able to penalize differences between neighbouring pixels when their amplitude is very small. This does not happen with quadratic priors that are based on differences between pixels, $g_i-g_{iv}$, and not on amplitude ratios, $g_i/g_{iv}$, on which the log-TV prior is based.

The log-TV Gibbs energy function is defined as follows

$$E_{\mathbf{G}}(\mathbf{G}) = \alpha \sum_{i,j,t} \sqrt{\log^2\left(\frac{g_{i,j}}{g_{i-1,j}}\right) + \log^2\left(\frac{g_{i,j}}{g_{i,j-1}}\right)} \tag{5}$$

and therefore the overall energy function to be minimized is

$$\mathbf{E}(\mathbf{G}, \lambda, \mathbf{Y}) = \sum_{i,j,t} \left[ g_{i,j} e^{-\lambda t} - y_{i,j,t} \log\left(g_{i,j} e^{-\lambda t}\right) \right] + \alpha L \sum_{i,j} \sqrt{\log^2\left(\frac{g_{i,j}}{g_{i-1,j}}\right) + \log^2\left(\frac{g_{i,j}}{g_{i,j-1}}\right)} \tag{6}$$

where α is a tuning parameter used to control the regularization strength that is kept constant in this step.

The minimization of the energy function (6) with respect to $g_{i,j}$ leads to a non-convex problem (Stephen Boyd & Lieven Vandenberghe, 2004) since it involves non-convex functions (e.g. $\sqrt{\log^2(x/a) + \log^2(x/b)}$). However, performing an appropriate change of variable, $s_{i,j} = \log(g_{i,j})$, it is possible to turn it into convex. Due to the monotonicity of the logarithmic function, the minimizers of both energy functions $\mathbf{E}(\mathbf{G}, \lambda, \mathbf{Y})$ and $\mathbf{E}(\mathbf{S}, \lambda, \mathbf{Y})$ are related by $\mathbf{S}^* = \log(\mathbf{G}^*)$.
The new objective function for the first step of this model is then

$$\mathbf{E}(\mathbf{S}, \lambda, \mathbf{Y}) = \sum_{i,j,t} \left[ e^{s_{i,j} - \lambda t} - y_{i,j,t}\left(s_{i,j} - \lambda t\right) \right] + \alpha L \sum_{i,j} \sqrt{\left(s_{i,j} - s_{i-1,j}\right)^2 + \left(s_{i,j} - s_{i,j-1}\right)^2} \tag{7}$$

The minimization of this equation is accomplished by finding its stationary points, performing iteratively its optimization in S with respect to each component $s_{i,j}$, one at a time, considering all other components in each iteration as constants.
Let us explicitly represent the terms involving a given node $s_{i,j}$ in the energy function (7)

$$\begin{aligned} \mathbf{E}(\mathbf{S}, \lambda, \mathbf{Y}) = & \sum_{t} \left[ e^{s_{i,j} - \lambda t} - y_{i,j,t} s_{i,j} \right] + \\ & \alpha L \left[ \sqrt{\left(s_{i,j} - s_{i-1,j}\right)^2 + \left(s_{i,j} - s_{i,j-1}\right)^2} + \sqrt{\left(s_{i+1,j} - s_{i,j}\right)^2 + \left(s_{i+1,j} - s_{i+1,j-1}\right)^2} + \right. \\ & \left. \sqrt{\left(s_{i,j+1} - s_{i-1,j+1}\right)^2 + \left(s_{i,j+1} - s_{i,j}\right)^2} \right] + C \end{aligned} \tag{8}$$

where C is a term that does not depend on $s_{i,j}$. To cope with the difficulty introduced by the non-quadratic terms, a Reweighted Least Squares based method is used (B.Wohlberg & P.Rodriguez, 2007). The minimizer of the convex energy function (8), $s^*$, is also the minimizer of the following energy function with quadratic terms

$$\begin{aligned}\mathbf{E}(\mathbf{S},\lambda,\mathbf{Y}) = &\sum_t\left[e^{s_{i,j}-\lambda t} - y_{i,j,t}s_{i,j}\right] + \\ &\alpha L\left[w\left(s^*_{i,j}\right)\left[\left(s_{i,j}-s_{i-1,j}\right)^2+\left(s_{i,j}-s_{i,j-1}\right)^2\right]+\right. \\ &w\left(s^*_{i+1,j}\right)\left[\left(s_{i+1,j}-s_{i,j}\right)^2+\left(s_{i+1,j}-s_{i+1,j-1}\right)^2\right]+ \\ &\left.w\left(s^*_{i,j+1}\right)\left[\left(s_{i,j+1}-s_{i-1,j+1}\right)^2+\left(s_{i,j+1}-s_{i,j}\right)^2\right]\right]+C\end{aligned} \tag{9}$$

where

$$w\left(s^*_{i,j}\right)=\frac{1}{\sqrt{\left(s^*_{i,j}-s^*_{i-1,j}\right)^2+\left(s^*_{i,j}-s^*_{i,j-1}\right)^2}} \tag{10}$$

Since the weights $w\left(s^*_{i,j}\right)$, $w\left(s^*_{i+1,j}\right)$ and $w\left(s^*_{i,j+1}\right)$ depend on the unknown minimizer $s^*_{i,j}$, an iterative procedure is used, where in the $k^{th}$ iteration, the estimated value $s^{(k-1)}_{i,j}$, computed in the previous iterations, is used instead of $s^*_{i,j}$. For sake of simplicity let us denote the weights $w\left(s^{(k-1)}_{i,j}\right)$, $w\left(s^{(k-1)}_{i+1,j}\right)$ and $w\left(s^{(k-1)}_{i,j+1}\right)$ just by $w, w_c$ and $w_d$ respectively. The minimization of (9) with respect to $s_{i,j}$ is performed by finding its stationary point,

$$\sum_t\left(e^{s_{i,j}-\lambda t} - y_{i,j,t}\right)+h_{i,j}=0 \tag{11}$$

where

$$h_{i,j}=2\alpha L\left[(2w+w_c+w_d)s_{i,j}-w\left(s_{i-1,j}+s_{i,j-1}\right)-w_c s_{i+1,j}-w_d s_{i,j+1}\right] \tag{12}$$

The minimizer of (7) with respect to $\lambda$ can be obtained through the computation of its stationary point, which is accomplished by solving the equation

$$\sum_{i,j,t}\left[-te^{s_{i,j}-\lambda t}+ty_{i,j,t}\right]=0 \tag{13}$$

Using the Newton's method the solutions of (11) and (13) can be iteratively obtained by

$$s^{(k+1)}_{i,j}=s^{(k)}_{i,j}-\frac{\sum_t\left(e^{s^{(k)}_{i,j}-\lambda t}-y_{i,j,t}\right)+h_{i,j}}{\sum_t\left(e^{s^{(k)}_{i,j}-\lambda t}\right)+2\alpha L(2w+w_c+w_d)} \tag{14}$$

$$\lambda^{(k+1)} = \lambda^{(k)} - \frac{\sum_{i,j,t}\left(-te^{s_{i,j}^{(k)}-\hat{\lambda}t} + ty_{i,j,t}\right)}{\sum_{i,j,t}\left(t^2 e^{s_{i,j}^{(k)}-\hat{\lambda}t}\right)} \tag{15}$$

The stopping criterion is based on the norm of the error of $\lambda$ between consecutive iterations and on the number of iterations. The norm of the error of $s_{i,j}$ was also computed but only for control purposes, since it acts as an auxiliary variable to estimate $\lambda$.

The estimated parameter $\hat{\lambda}$ is used in the next step as a constant, under the assumption that the intensity decay due the *photobleaching* effect was totally caught in this step.

### 2.2 Step two

The ultimate goal of the second step of the proposed algorithm is to estimate the time and space varying cell nucleus morphology, denoted by $\mathbf{F} = \{f_{i,j,t}\}$, where the intensity decay rate due the *photobleaching* is characterized by the parameter $\lambda$ estimated in the previous step. Each point of the noiseless image sequence, $\mathbf{X} = \{x_{i,j,t}\}$ to be estimated is defined in this step as

$$x_{i,j,t} = f_{i,j,t}\ e^{-\hat{\lambda}t} \tag{16}$$

The estimation of the parameters $f_{i,j,t}$, performed in a Bayesian framework by using the maximum *a posteriori* (MAP) criterion, may be formulated as the following optimization task

$$\hat{\mathbf{F}} = \arg\min_{\mathbf{F}}\ \mathbf{E}\left(\mathbf{F}, \hat{\lambda}, \mathbf{Y}\right) \tag{17}$$

where the energy function $\mathbf{E}(\mathbf{F}, \hat{\lambda}, \mathbf{Y}) = \mathbf{E}_{\mathbf{Y}}(\mathbf{F}, \hat{\lambda}, \mathbf{Y}) + \mathbf{E}_{\mathbf{F}}(\mathbf{F})$, as before, is the sum of two terms, $\mathbf{E}_{\mathbf{Y}}(\mathbf{F}, \hat{\lambda}, \mathbf{Y})$, the data fidelity term and $\mathbf{E}_{\mathbf{F}}(\mathbf{F})$, the energy associated to the *a priori* distribution for $\mathbf{F}$.

To preserve the edges of the cell morphology, log-TV and $L_1$ ($L_1$ norm) potential functions are used in space and in time respectively. The regularization is performed simultaneously in the image space and in time using different prior parameters which means that this denoising iterative algorithm involves an anisotropic 3-D filtering process that is able to accomplish different smoothing effects in the space and in the time dimensions.

The energy function related to the a priori distribution of $\mathbf{F}$ is given by

$$E_{\mathbf{F}}(\mathbf{F}) = \alpha \sum_{i,j,t} \sqrt{\log^2\left(\frac{f_{i,j,t}}{f_{i-1,j,t}}\right) + \log^2\left(\frac{f_{i,j,t}}{f_{i,j-1,t}}\right)} + \beta \sum_{i,j,t} \left|\log\left(\frac{f_{i,j,t}}{f_{i,j,t-1}}\right)\right| \tag{18}$$

Therefore the overall problem consists on minimizing the following function

$$\begin{aligned}\mathbf{E}(\mathbf{F},\hat{\lambda},\mathbf{Y}) = &\sum_{i,j,t}\left[f_{i,j,t}e^{-\hat{\lambda}t} - y_{i,j,t}\log\left(f_{i,j,t}e^{-\hat{\lambda}t}\right)\right]\\ &+\alpha\sum_{i,j,t}\sqrt{\left(\log\left(f_{i,j,t}\right)-\log\left(f_{i-1,j,t}\right)\right)^2+\left(\log\left(f_{i,j,t}\right)-\log\left(f_{i,j-1,t}\right)\right)^2}\\ &+\beta\sum_{i,j,t}\left|\log\left(f_{i,j,t}\right)-\log\left(f_{i,j,t-1}\right)\right|\end{aligned} \tag{19}$$

where $\alpha$ and $\beta$ are tuning parameters to control the strength of the regularization in space and in time respectively. The parameter $\alpha$ is adaptive and $\beta$ is constant. The standard deviation of the logarithm of the morphology, computed for each image, seems to perform an important role in adapting the strength of the regularization in the space domain. Thus, for both synthetic and real data, $\alpha = \alpha_0 \times \mathrm{std}(\log(f_{i,j,t}))$, where $\alpha_0$ is a constant, is used.

As before, in the previous step, the energy function (19) with respect to $f_{i,j,t}$ is non convex. Once again, to make it convex, the following change of variable is performed: $z_{i,j,t} = \log(f_{i,j,t})$. Due to the monotonicity of this function, the minimizer of $\mathbf{E}(\mathbf{F},\hat{\lambda},\mathbf{Y})$ is related to the one of $\mathbf{E}(\mathbf{Z},\hat{\lambda},\mathbf{Y})$ by $\mathbf{Z}^* = \log(\mathbf{F}^*)$, where the log function of tensor $\mathbf{F}$ is taken component-wise.

The objective function to be minimized with respect to the unknowns $z_{i,j,t}$ in this second step is

$$\begin{aligned}\mathbf{E}(\mathbf{Z},\hat{\lambda},\mathbf{Y}) = &\sum_{i,j,t}\left[e^{z_{i,j,t}-\hat{\lambda}t} - y_{i,j,t}\left(z_{i,j,t}-\hat{\lambda}t\right)\right]+\\ &\alpha L\sum_{i,j,t}\sqrt{\left(z_{i,j,t}-z_{i-1,j,t}\right)^2+\left(z_{i,j,t}-z_{i,j-1,t}\right)^2}+\\ &\beta L\sum_{i,j,t}\left|z_{i,j,t}-z_{i,j,t-1}\right|\end{aligned} \tag{20}$$

The estimation of $\mathbf{Z}$ is performed by using the ICM (Iterated Conditional Modes) method (J.Besag, 1986) where (20) is minimized with respect to each unknown $z_{i,j,t}$ at a time, keeping all other unknowns constant.

As before, let us consider explicitly the terms involving a given node $z_{i,j,t}$ in the energy equation

$$\begin{aligned}E(\tilde{Z},\lambda,Y) = &\sum_t\left[e^{z_{i,j,t}-\hat{\lambda}t}+y_{i,j,t}z_{i,j,t}\right]+\alpha L\sqrt{\left(z_{i,j,t}-z_{i-1,j,t}\right)^2+\left(z_{i,j,t}-z_{i,j-1,t}\right)^2}+\\ &\sqrt{\left(z_{i+1,j,t}-z_{i,j,t}\right)^2+\left(z_{i+1,j,t}-z_{i+1,j-1,t}\right)^2}+\\ &\sqrt{\left(z_{i,j+1,t}-z_{i-1,j+1,t}\right)^2+\left(z_{i,j+1,t}-z_{i,j,t}\right)^2}+\\ &\beta\left[\left|z_{i,j,t}-z_{i,j,t-1}\right|+\left|z_{i,j,t+1}-z_{i,j,t}\right|\right]+C\end{aligned} \tag{21}$$

where C is a term that does not depend on $z_{i,j,t}$. The optimization of (21) is performed by using the Reweighted Least Squares method, as before in the first step, to cope with the non quadratic prior terms. The minimizer of the convex energy function (21), $\mathbf{Z}^*$,is also the minimizer of the following energy function with quadratic terms

$$\begin{aligned}\mathbf{E}(\mathbf{Z},\lambda,\mathbf{Y}) = \sum_t \Big[ e^{z_{i,j,t}-\hat{\lambda}t} - y_{i,j,t}z_{i,j,t} \Big] + \\ \alpha \Big[ w\left(z^*_{i,j,t}\right)\Big[\left(z_{i,j,t}-z_{i-1,j,t}\right)^2+\left(z_{i,j,t}-z_{i,j-1,t}\right)^2\Big] + \\ w\left(z^*_{i+1,j,t}\right)\Big[\left(z_{i+1,j,t}-z_{i,j,t}\right)^2+\left(z_{i+1,j,t}-z_{i+1,j-1,t}\right)^2\Big] + \\ w\left(z^*_{i,j+1,t}\right)\Big[\left(z_{i,j+1,t}-z_{i-1,j+1,t}\right)^2+\left(z_{i,j+1,t}-z_{i,j,t}\right)^2\Big]\Big] + \\ \beta\Big[ v(z_{i,j+1,t})\left(z_{i,j,t}-z_{i,j,t-1}\right)^2 + v(z_{i,j,t+1})\left(z_{i,j,t+1}-z_{i,j,t}\right)^2\Big] + C\end{aligned} \tag{22}$$

where

$$w\left(z^*_{i,j,t}\right) = \frac{1}{\sqrt{\left(z^*_{i,j,t}-z^*_{i-1,j,t}\right)^2+\left(z^*_{i,j,t}-z^*_{i,j-1,t}\right)^2}}\ , \tag{23}$$

and

$$v\left(z^*_{i,j,t}\right) = \frac{1}{\left|z^*_{i,j,t}-z^*_{i,j,t-1}\right|} \tag{24}$$

Since the weights $w\left(z^*_{i,j,t}\right)$, $w\left(z^*_{i+1,j,t}\right)$, $w\left(z^*_{i,j+1,t}\right)$ , $v\left(z^*_{i,j,t}\right)$ and $v\left(z^*_{i,j,t+1}\right)$ depend on the unknown minimizer $\mathbf{Z}^*$, the same iterative procedure used in the first step is adopted here, where the estimation of $\mathbf{Z}^*$ at the previous $(k-1)^{th}$ iteration, $\mathbf{Z}^{(k-1)}$, is used. Let us denote these weights by $w, w_c, w_d, v_a$ and $v_c$ respectively.

The minimization of (22) with respect to $z_{i,j,t}$ is obtained by finding its stationary point,

$$\frac{\partial E(\mathbf{Z},\lambda,\mathbf{Y})}{\partial z_{i,j}} = e^{z_{i,j}-\hat{\lambda}t} - y_{i,j,t} + h_{i,j,t} = 0 \tag{25}$$

where

$$\begin{aligned}h_{i,j,t} = 2\left(2\alpha w + \alpha w_c + \alpha w_d + \beta v_a + \beta v_c\right)z_{i,j,t} - 2\alpha w\left(z_{i-1,j,t}+z_{i,j-1,t}\right) - 2\alpha w_c z_{i+1,j,t} - \\ 2\alpha w_d z_{i,j+1,t} - 2\beta\left(v_a z_{i,j,t-1} + v_c z_{i,j,t+1}\right)\end{aligned} \tag{26}$$

Using the Newton's method the solution of (25) can be obtained iteratively by

$$z^{(k+1)}_{i,j,t} = z^{(k)}_{i,j,t} - \frac{e^{z_{i,j,t}-\hat{\lambda}t} - y_{i,j,t} + h_{i,j,t}}{e^{z_{i,j,t}-\hat{\lambda}t} + 2\alpha\left(2w + w_c + w_d\right) + 2\beta\left(v_a + v_c\right)} \tag{27}$$

## 3. Experimental Results

In this section experimental results with synthetic and real data are presented.

### 3.1 Synthetic data

The synthetic data is formed by a set of 64 images of a white circle moving from the left top corner of the first image down to the right, along the diagonals of 64 squares, 64×64 pixels, with constant velocity, over a grey background. This set of images was conceived having in mind the real situation where the morphology of a cell nucleus changes along the image with time. For the first image of the sequence (t=0), the intensities of the circle and of the background were set equal to 50 and 10 respectively. The final sequence of synthetic data was then generated by applying an exponential decay in time (t=0,…,63) with rate equal to $\lambda$=0.025 image$^{-1}$ , followed by corruption with Poisson noise. This rate of decay can be considered realistic under the hypothesis of an acquisition rate of 10s, which means $\lambda$=0.0025s$^{-1}$ .

Fig. 1 shows images for three time instants of the synthetic sequence. The images on the first double row (a) belong to the original sequence, before being corrupted by Poisson noise. The same images corrupted with Poisson noise are shown in (b). The third double row (c), with the results of the reconstruction according to eq. 16 of the second step of the algorithm, show the ability of this methodology for removing noise, although providing good preservation of the edges of the moving circle.

(a)

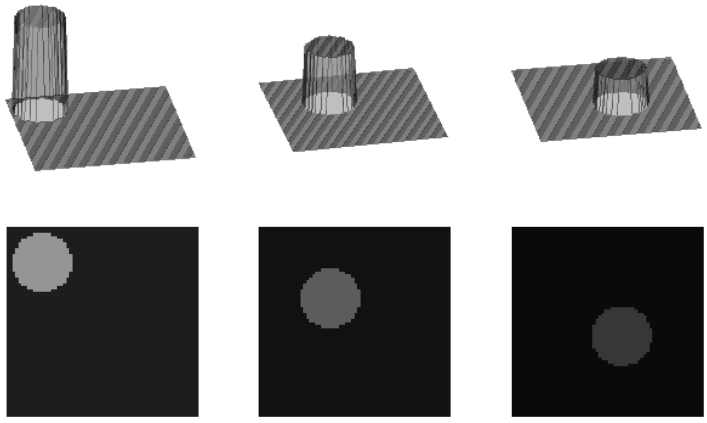

(b)

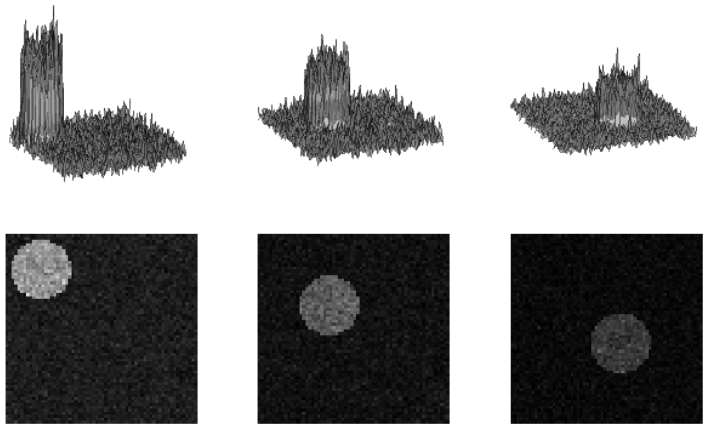

(c)

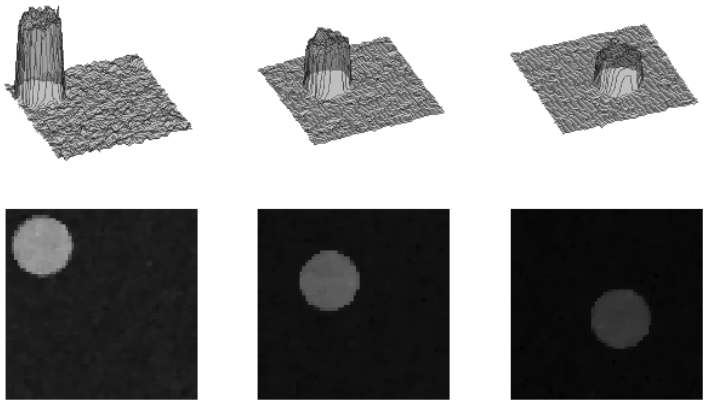

Fig. 1. (a),(b),(c) Three time instants (1, 20, 40) of the true, noisy and reconstructed synthetic sequences and respective mesh representations.

The mesh representations of the estimated morphology for three different time instants of the sequence show the ability of the algorithm to recover the true morphology whose shape is a constant height cylinder and whose behaviour in time is to slide down along the diagonal of a $64 \times 64$ pixels square. Both the position and the height of the cylinder are correctly estimated for the complete sequence.

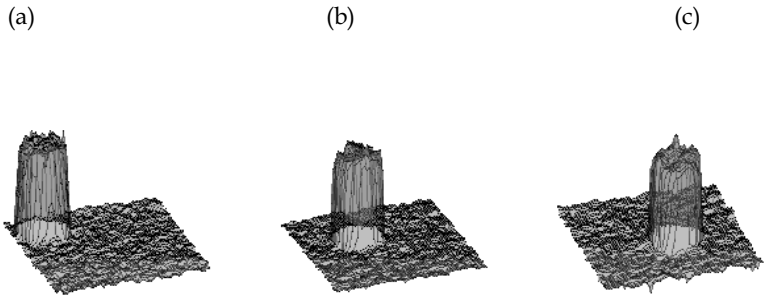


Fig. 2. Mesh representation of the estimated morphology $\hat{f}_{i,j,t}$ for images 1 (a), 20 (b) and 40 (c).

An example of the denoising and recovery capabilities of the presented methodology is shown in Fig. 3. where the true (a), the noisy (b) and the estimated (c) morphologies corresponding to image 48 of the sequence are displayed. Subplot (d) shows profiles taken along the diagonal of (a), (b) and (c). In spite of the degradation of the image, it is noticeable how well the algorithm manages to recover the morphology.

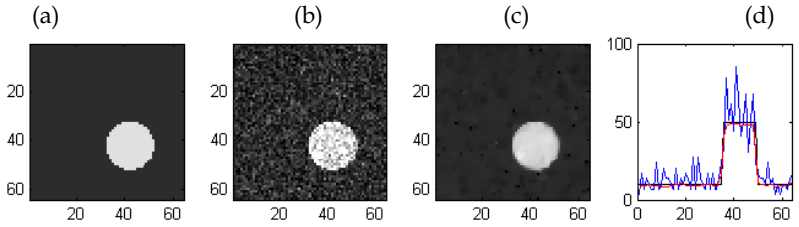


Fig. 3. (d) Morphology profiles, image 48, (a) True (black line in (d)), (b) Noisy (blue line in (d)), (c) Estimated (red line in (d)).

The root mean square error (RMSE) of the estimated morphology of the complete sequence was computed for each of the 300 iteration of the second step and its plot can be seen in Fig. 4. During the first 20 iterations the RMSE drops very quickly and keeps that trend till the end of the iterative procedure, which suggests effective convergence of the algorithm.

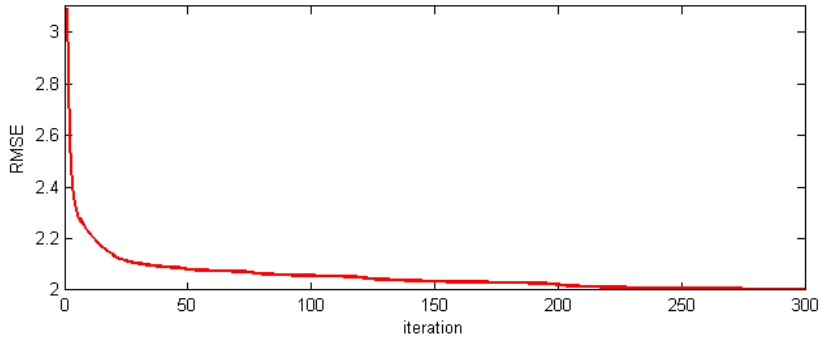


Fig. 4. Root mean square error (RMSE) of the estimated morphology of the complete sequence, in every iteration.

In order to evaluate the quality of the presented algorithm, the *signal to noise ratio* (SNR), the *mean square error* (MSE) and the *Csiszáér I-divergence* (I-div) were adopted. The literature is not very conclusive on what concerns to the choice of the *figure of merit* more suitable to evaluate the quality of an algorithm that deals with Poisson multiplicative noise.
Some authors use the SNR although there is strong evidence that it gives a more efficient quality evaluation in the Gaussian denoising situations than in the Poissonian ones.
As in section 2, let $X = \{x_{i,j,t}\}$ and $\hat{X} = \{\hat{x}_{i,j,t}\}$ with $0 \le i, j,t \le N-1, M-1, L-1$, be respectively the noiseless and the estimated sequences of images. The SNR of image t of the estimated sequence can be defined as:

$$SNR(t) = 10\log_{10}\left(\frac{\sum_{i,j}\left(x_{i,j,t}\right)^2}{\sum_{i,j}\left(x_{i,j,t}-\hat{x}_{i,j,t}\right)^2}\right) \quad 28$$

The MSE is extensively used with the purpose of evaluating the quality of the denoising algorithm, independently of the noise statistics and is defined as:

$$MSE(t) = \frac{1}{MN}\sum_{i,j}\left(x_{i,j,t}-\hat{x}_{i,j,t}\right)^2 \quad 29$$

According to (N. Dey et al., 2004), to quantify the quality of the denoising procedure in the presence of non-negativity constraints, which is the case of the Poisson denoising, the Csiszáér I-divergence (Csiszáér, 1991) is the best choice.
The I-Divergence between the $t^{th}$ image of the original (noiseless) sequence X and the $t^{th}$ image of the restored sequence $\hat{X}$ is given by:

$$I\_div_{X,\hat{X}}(t) = \sum_{i,j}\left[x_{i,j,t}\log\left(\frac{x_{i,j,t}}{\hat{x}_{i,j,t}}\right) - \left(x_{i,j,t}-\hat{x}_{i,j,t}\right)\right] \quad 30$$

The I-Divergence can be interpreted as a quantifier of the difference between the true image and the estimated one. Ideally, a perfect denoising should end with an I-div equal to zero.

A Monte Carlo experiment with 500 runs, based on sequences similar to the described above, was carried out. For each run, the rate of decay $\lambda$ was estimated in the first step and used to estimate the morphology $f_{i,j,t}$ in the second step. The final reconstruction is obtained by $\hat{x}_{i,j,t} = \hat{f}_{i,j,t} e^{-\hat{\lambda} t}$.

The SNR, the MSE and the I-div were computed for every image in each of the 500 runs and the means and standard deviations of the estimated lambda, $\hat{\lambda}^{(run)}$, of the SNR of the reconstruction, $SNR_{\hat{X}}^{(run)}$, of the MSE of the morphology, $MSE_{\hat{F}}^{(run)}$, of the MSE of the reconstruction, $MSE_{\hat{X}}^{(run)}$, of the I-div of the morphology, $I-div_{\hat{F}}^{(run)}$ and of the I-div of the reconstruction $I-div_{\hat{X}}^{(run)}$, were computed.

The mean of the estimated rate of decay is 0.025061, with a mean square error (MSE) of 0.00011126, which is very close to the original one (0.025) .

Fig. 5. (a) shows the mean of the SNR for each image of the noisy sequences used in the Monte Carlo experiment (black line) and the mean of the SNR of the respective reconstruction. As can be noticed, the SNR improvement is $\approx 10dB$ and is almost constant throughout the sequence of images.

The mean of the MSE of the reconstruction is plotted in Fig. 5. (b) strengthen the evidence of the ability of the presented algorithm to restore this type of sequences.

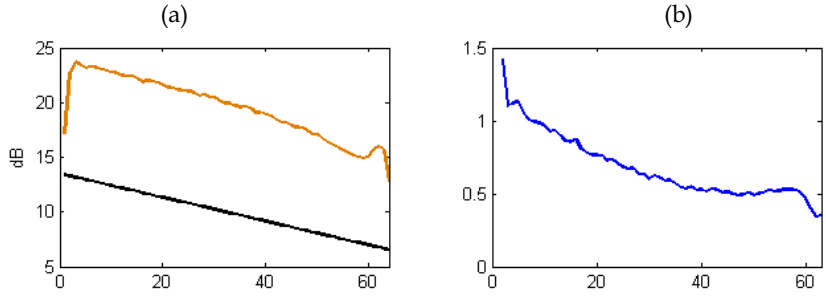


Fig. 5 (a) Mean of the SNR over the 500 runs computed from the noisy sequence (black line) and from the reconstructed sequence $\hat{X}$ (red line), (b) Mean of the MSE of the reconstructed sequence.

In the present situation the mean of the I-div of the reconstructed images (Fig. 6.) is not zero as it would be in an ideal case, but it is well bellow the one obtained with the noisy sequences.

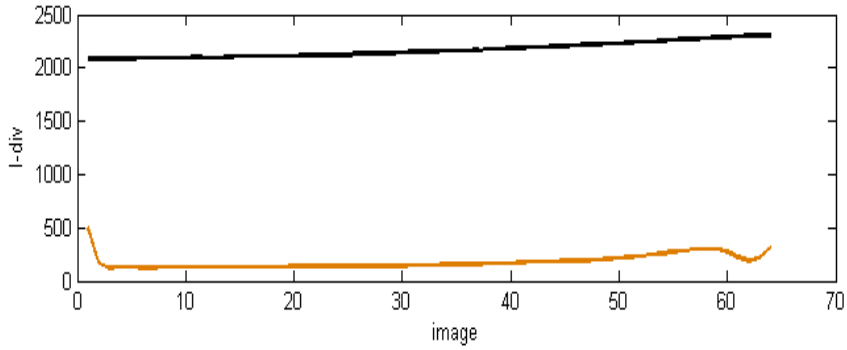


Fig. 6. I-div mean over 500 runs from the noisy sequence y (black line) from the reconstructed sequence $\hat{X}$ (red line).

### 3.2 Real data

Three sets of real CLSFM images of cell nucleus, identified as 2G100, 7GREEN_FRAP and BDM_FLIP, were analyzed.

The sequence 2G100 consists of 100 CLSFM images of a Hela cell nucleus, acquired at a rate of 23s, in normal laboratory conditions, using a continuous, low intensity laser illumination. During the acquisition of the 2G100 sequence, no additional techniques such as FRAP (Fluorescence Recovery After Photobleaching) or FLIP (Fluorescence Loss In Photobleaching) were employed. The aim is the observation of a cell nucleus where certain particles are tagged with fluorescent proteins, for quite a long time, in order to acquire data where the *photobleaching* effect occurs without the interference of important diffusion and transport phenomena.

Three images, 1, 20, 45 of this sequence, corresponding to the time instants 0s, 460s and 1035s after the beginning of the acquisition process, are displayed in Fig. 7. (a), (b) and (c). The appearance of these images is noisy, with an SNR decreasing very quickly with the time.

Using the previously described methodology, the rate of decay due to the *photobleaching*, $\lambda$, and the cell nucleus morphology, $F_{i,j,t} = \{f_{i,j,t}\}$, were estimated. The achieved value for the rate of decay was $\hat{\lambda} = 3.9988 \times 10^{-4}\,s^{-1}$.

Fig. 8. (a), (b) and (c) show images of the reconstructed sequence for the same time instants as in Fig. 7, where a considerable reduction of noise can be observed while their morphological details are preserved.

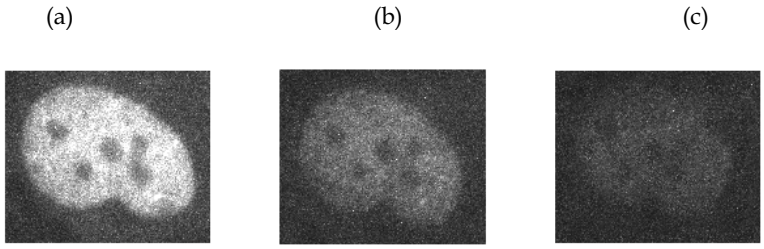


Fig. 7. Noisy images 1 (a), 20 (b), 45 (c) from the real data set 2G100.

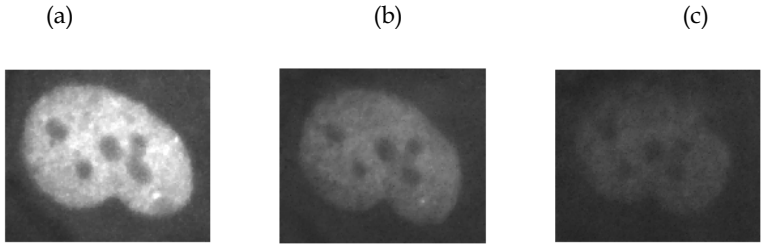


Fig. 8. Images 1 (a), 20 (b), 45 (c) from reconstructed sequence (2G100).

Three images of the estimated morphology can be seen in Fig. 9. (a), (b) and (c). It is noticeable the substantial improvement in the quality of the details of the cell nucleus structure. In particular, the comparison between the images displayed in Fig.7.c) and Fig.9.c) reveals the ability of the algorithm to recover information from original images where almost no information is available.

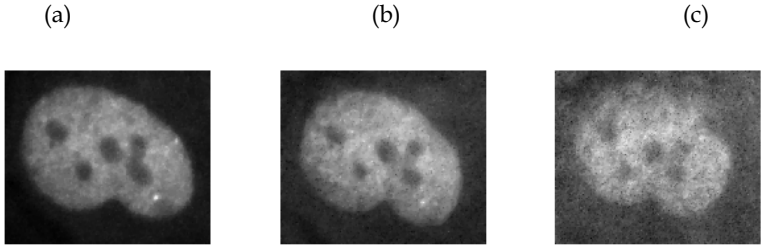


Fig. 9. Estimated morphology corresponding to images 1 (a), 20 (b), 45 (c) of the data set 2G100.

The plot of the horizontal and vertical profiles along the dashed lines in image (Fig. 10. (a), (b) and (c)) reinforces this idea. The intensity valleys become more perceptible and identifiable. The noise undergoes an effective reduction and the edges are well defined and preserved.

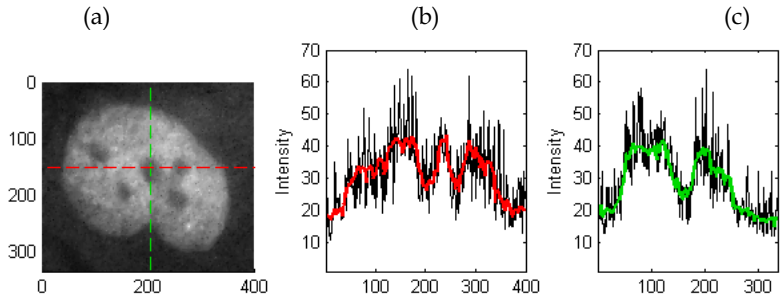


Fig. 10. (a) Reconstructed image 20 of the sequence 2G100. The red dash line corresponds to the horizontal profile in (b). The green dashed line stands for the vertical profile in (c).

The means and standard deviations (std) of the images of the noisy and reconstructed sequences were computed and the results are presented in the plot of Fig. 11. (a) and (b). As can be observed in (a), the mean of the images is well preserved in the reconstruction; in addition, the pattern of the std becomes smoother.

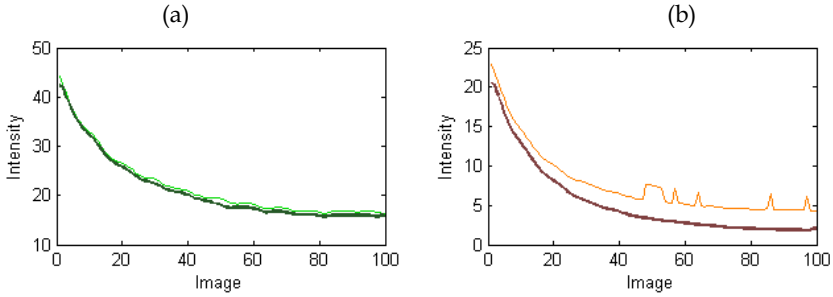


Fig. 11. (a) Mean of each image of the sequence 2G100. Dark and light green lines correspond to the reconstructed and to the noisy sequences respectively. (b) Standard deviation of each image of the sequence 2G100. Dark and light red lines correspond to the reconstructed and to the noisy sequences respectively.

In order to test the behaviour of the proposed algorithm in more complex situations where diffusion and transport phenomena are present, the sequences 7GREEN_FRAP and BDM_FLIP are used.

Sequence 7GREEN_FRAP consists of 108 images acquired at a rate of 9.4s *per* image, using the FRAP (Fluorescence Recovery After Photobleaching) technique (R. Underwood, 2007). In this technique a pre-defined region in the cell is illuminated with a high intensity focused laser beam, during a small period of time, to force the irreversible *photobleaching* of the fluorescence tagged molecules present within that region. The movements of the bleached molecules out of the bleached region and of the surrounding unbleached molecules into the bleached area lead to a recovery of fluorescence into the bleached area. The acquisition

process consists on monitoring this recovery over time, at low laser power, to prevent further bleaching. In this situation the fluorescence recovery superimposes the global *photobleaching* due to the low intensity illumination of the cell nucleus, which explains the slight increase of the intensity with the time.
As expected, the estimated rate of decay is negligible. Eventual small intensity fluctuations that may be observed in the images are due to the manual fine tuning required to keep the target points in focus during the experiment.

In Fig. 12. (a), (b) and (c) and Fig. 13. (a), (b) and (c), images corresponding to the time instants t=9.4s, 460.6s and 1005.8s of the raw data and of the reconstruction are shown. Also the corresponding estimated morphology is presented in Fig. 14. (a), (b) and (c). These images denote a substantial improvement in the details of the nucleus structure.

(a) (b) (c)

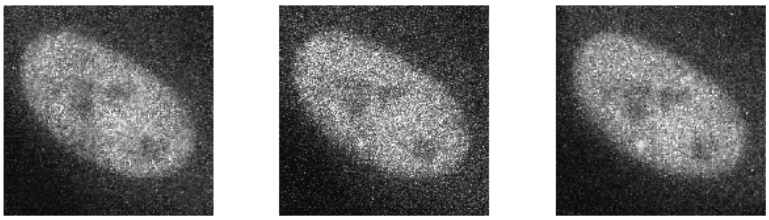

Fig. 12. (a) Noisy images 2 (a), 50 (b), 108 (c), real data set 7GREEN_FRAP.

(a) (b) (c)

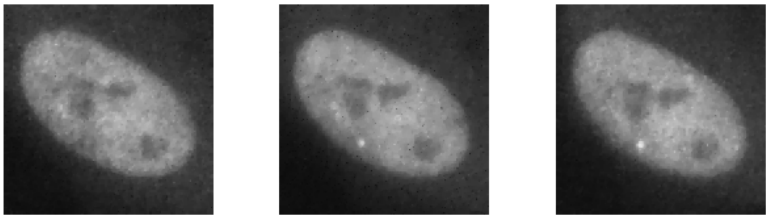

Fig. 13. Reconstructed images 2 (a), 50 (b), 108 (c), sequence 7GREEN_FRAP.

(a) (b) (c)

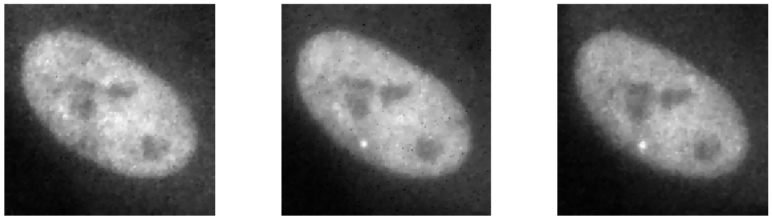

Fig. 14. (a) Morphology 2 (a), 50 (b), 108 (c), sequence 7GREEN_FRAP.

The profiles in Fig. 15. (a), (b) and (c) confirm this assertion. In this figure two images and respective profiles are displayed to illustrate the increase of the intensity with time.

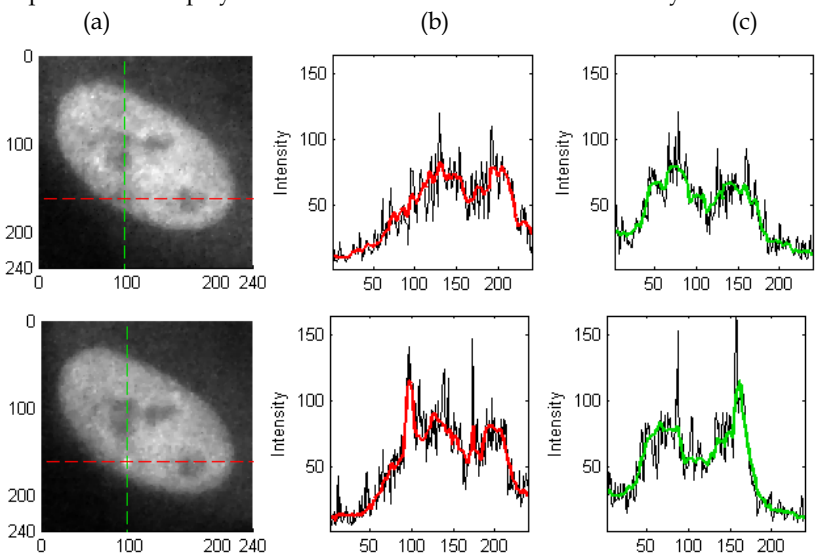


Fig. 15. (a) Reconstructed image 2 (first row) and 108 (second row) of the sequence 7GREEN_FRAP. The red dash line corresponds to the horizontal profile in (b). The green dashed line stands for the vertical profile in (c).

Plots of the intensity means of the noisy and of the reconstructed sequences show the constancy characteristic of an almost zero rate of decay. In addition, the reconstruction mean (Fig.16. (a)), is well preserved while the std (Fig. 16. (b)) is smoother than the corresponding to the noisy sequence.

From all these assertions it is possible to assume that the presented methodology is appropriate for denoising and for morphology estimation when the FRAP technique is used.

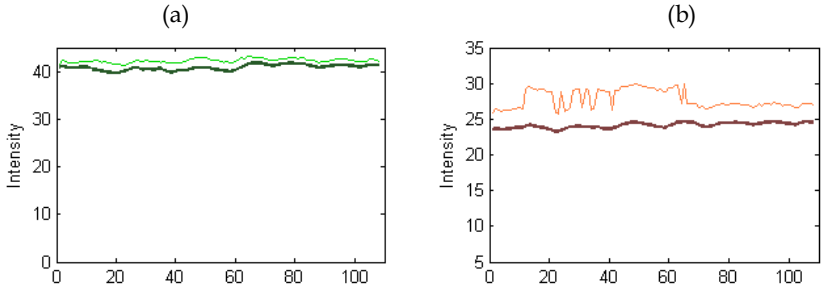


Fig. 16. (a) Mean of each image of the sequence 7GREEN_FRAP. Dark and light green lines correspond to the reconstructed and to the noisy sequences respectively. (b) Standard deviation of each image of the sequence 7GREEN_FRAP. Dark and light red lines correspond to the reconstructed and to the noisy sequences respectively.

The BDM_FLIP sequence consists of 175 images acquired at a rate of 7.4s and is the result of applying the FLIP (Fluorescence Loss In Photobleaching) technique (R.Underwood, 2007)to the Hela cell nucleus. This technique makes use of the *photobleaching* effect as a perturbing agent of the distribution of fluorescent molecules in the cell nucleus. In a FLIP experiment, during a certain time interval, a small defined region within the nucleus, expressing fluorescently tagged proteins, is illuminated with repetitive bleach pulses of a high intensity focused laser beam, in order to force the occurrence of the *photobleaching* effect. The surrounding area is then monitored for a decrease in the level of fluorescence. Any fraction of the cell nucleus connected to the area being bleached will gradually fade owing to the movement of bleached molecules into the bleached region. The resulting information from the experiment can then be used to determine the kinetic properties, including diffusion coefficients, mobile fraction and transport rate of the fluorescently labeled molecules.
Three images from the sequence (t=29.6s, t=362.6s and t=843.6s) and respective reconstruction are displayed in Figs. 17. (a), (b) and (c) and Figs. 18. (a), (b) and (c). It is easy to perceive that the intensity decrease is quite fast which is very inconvenient when the acquisition times are long.

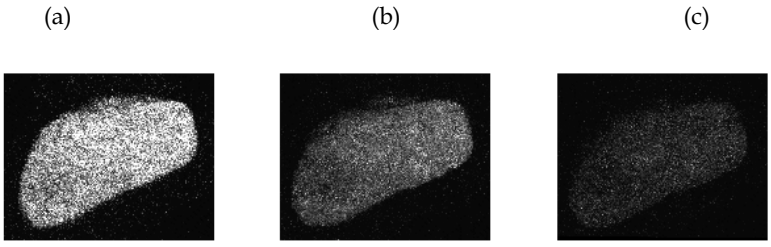


Fig. 17. (a) Noisy images 5 (a), 50 (b), 115 (c), real data set BDM_FLIP.

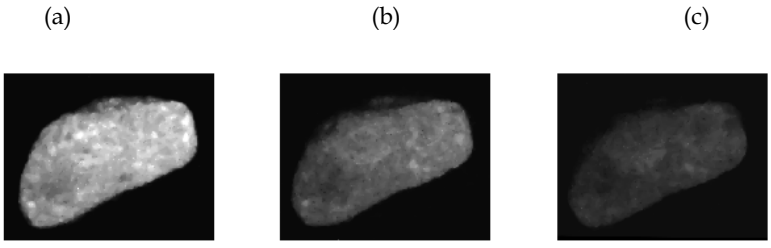


Fig. 18. (a) Reconstructed images 5 (a), 50 (b), 115 (c), sequence BDM_FLIP.

The estimated value of the rate of decay of the intensity is $\hat{\lambda} = 1.5 \times 10^{-3}\,\mathrm{s}^{-1}$. This value is obviously larger than the one obtained for the sequence 2G100, due to the use of the FLIP technique that reinforces the decrease of the intensity.
The estimated morphology is shown in Fig. 19. (a), (b) and (c) and the improvement in the details of the nucleus structure are noticeable.

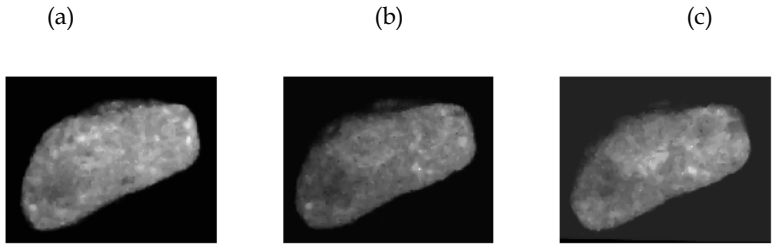


Fig. 19. (a) Morphology images 5 (a), 50 (b), 115 (c), BDM_FLIP.

The profiles in Fig. 20. (a), (b) and (c) were chosen to show the bleached region of the nucleus. This region can be identified in the profiles as a depression of the intensity.

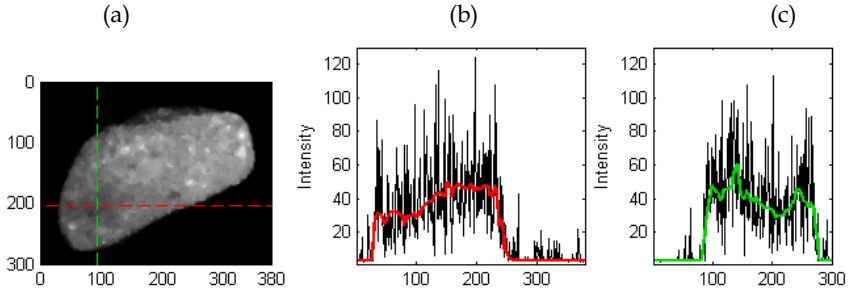


Fig. 20. (a) Reconstructed image 10 of the sequence BDM_FLIP. The red dash line corresponds to the horizontal profile in (b). The green dashed line stands for the vertical profile in (c).

The mean of the reconstruction (Fig. 21. (a)) is preserved and the std (Fig. 21. (b)) is smoothed.

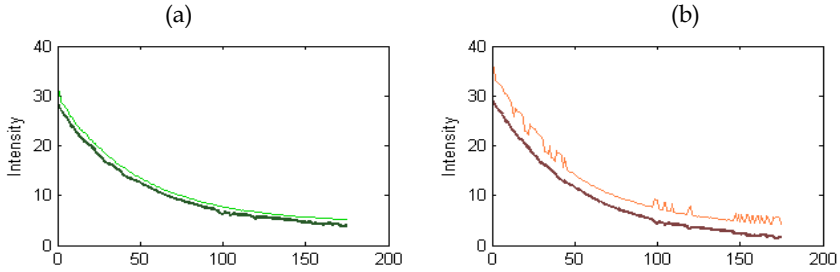


Fig. 21. (a) Mean of each image of the sequence BDM_FLIP. Dark and light green lines correspond to the reconstructed and to the noisy sequences respectively. (b) Standard deviation of each image of the sequence BDM_FLIP. Dark and light red lines correspond to the reconstructed and to the noisy sequences respectively.

## 4. Conclusion

In this chapter a new denoising algorithm for fluorescence microscopy (FM) imaging, to deal with the Poissonian multiplicative noise corrupting the images, is proposed. Furthermore, image sequences acquired along the time present an intensity decreasing due to the permanent fluorophore loss of its ability to fluoresce. This effect is caused by photochemical activity induced by the incident light that favours reactions of the fluorescent protein with other surrounding molecules. This intensity decrease prevents long time acquisition experiments because of the lack of morphological details in the last images of the sequence, making the biological information recovery a difficult task.

The proposed algorithm is designed in the Bayesian framework, as an optimization task, with the maximum *a posteriori* (MAP) criterion. The observation model takes into account the *photobleaching* effect in order to recover as much as possible all the information present in the sequence, even from the last images exhibiting a very low *signal to noise ratio* (SNR). This is possible because the algorithm establishes temporal correlation between consecutive images within the sequence.

The algorithm is developed iteratively in two steps. The intensity decay rate due to the *photobleaching* is estimated in the first step assuming a time invariant cell morphology. The goal in this step is to capture exclusively the intensity time variation caused by the *photobleaching* in the exponential term. In the second step the time and space varying cell morphology is estimated after compensating the *photobleaching* effect with the decay rate estimated in the first step.

The energy functions used in the optimization problem are designed to be convex and their minimizers are computed by using the Newton's algorithm and a reweighted least squares based method. This approach guarantees a continuous convergence towards the global minimum. Furthermore, the prior distributions needed to regularize the solutions use edge preserving potential functions. The associated Gibbs energy function is based on log-Euclidean total variation functions in time and in space, appropriated to this positively constrained optimization problem.

Monte Carlo tests with synthetic data were used to assess the performance of the algorithm. These tests have shown the ability of the algorithm to strongly reduce the Poisson multiplicative noise, to estimate both the decay rate due to the *photobleaching* and the underlying morphology and, simultaneously, to preserve the transitions.

Tests with real data from *laser scanning fluorescence confocal microscopy* were also performed where it is shown the effectiveness of the algorithm to cope with this type of noise and low SNR, even when the FRAP and FLIP techniques are used. Images and profiles extracted from the original and processed images are displayed for visualization and comparison purposes.

## 5. Acknowledgment

The authors thank Dr. José Rino and Profª Maria do Carmo Fonseca, from the Instituto de Medicina Molecular, Faculdade de Medicina da Universidade de Lisboa, for providing biological technical support and the real data used in this paper.
This work was supported by Fundação para a Ciência e a Tecnologia (ISR/IST plurianual funding) through the POS Conhecimento Program which includes FEDER funds.

## 6. References

Arsigny, V.; Fillard, P.; Pennec X. & Ayache N. (2006). Log-Euclidean metrics for fast and simple calculus on diffusion tensors, *Magnetic Resonance in Medicine*, vol. 56, no. 2, pp. 411–421, August 2006.

Bardsley, J. & Luttman, A. (2006). Total variation-penalized Poisson likelihood estimation for ill-posed problems, Depart. Math Sci., Univ. Montana Missoula, Tech. Rep. 8, 2006.

Besag, J. (1986). On the statistical analysis of dirty pictures, *J. R. Statist. Soc. B*, vol. 48, no. 3, pp. 259–302, 1986.

Besbeas, P.; Italia De Feis & Sapatinas T. (2004). A comparative simulation study of wavelet shrinkage estimators for Poisson counts., *Int. Stat. Rev.*, vol. 72, no. 2, pp. 209–237, 2004.

Boulanger, J.; Sibarita, J.-B.; Kervrann, C.; Bouthemy P. (2008). Non-Parametric regression for patch-based fluorescence microscopy image sequence denoising, *Proc. IEEE Int. Symp. on Biomedical Imaging, ISBI'08*, , pp. 748-751, Paris, France, May, 2008.

Boyd, S. & Vandenberghe, L. (2004). *Convex Optimization*. Cambridge University Press.

Braga, J.; Desterro, J.M. & Carmo-Fonseca; M. (2004). Intracellular macromolecular mobility measured by fluorescence recovery after photobleaching with confocal laser scanning microscopes. *Mol Biol Cell.*, 15:4749-60.

Csiszáér, I. (1991)., Why least squares and maximum entropy? an axiomatic approach to inference for linear inverse problems, *The Annals of Statistics*, vol. 19, no. 4, pp. 2032–2066, 1991.

Dey, N., Blanc- Féraud, L.; Zimmer, C.; Kam, Z.; Olivo-Marin, J.-C. & Zerubia J. (2004). A deconvolution method for confocal microscopy with total variation regularization, *IEEE International Symposium on Biomedical Imaging: Nano to Macro, 2004*, vol. 2, pp. 1223–1226, April 2004.

Dey, N.; Blanc- Féraud, L.; Zimmer, C.; Roux, P.; Kam, Z.; Olivo-Marin, J.-C. & Zerubia, J. (2006). "Richardson–Lucy Algorithm With Total Variation Regularization for 3D Confocal Microscope Deconvolution", Microcopy Research and Technique, 69:260-266, 2006.

Dupé, F.X.; Fadili, M.J.; Starck, J-L. (2008). Deconvolution of confocal microscopy images using proximal iteration and sparse representations, *ISBI 2008*, Paris, France, 2008.

Fisz, M. (1955). The limiting distribution of a function of two independent random variables and its statistical application, *Colloquium Mathematicum,*, vol. 3, pp. 138 – 146, 1955.

Fryźlewicz, P. & Nason, G. (2001)., Poisson intensity estimation using wavelets and the Fisz transformation, Department of Mathematics, University of Bristol, United Kingdom, Tech. Rep. 01/10, 2001.

Geman S. & Geman, D. (1984). Stochastic relaxation, Gibbs distributions, and the Bayesian restoration of images, *IEEE Transactions on Pattern Analysis and Machine Intelligence*, vol. PAMI, no. 6, pp. 721–741, Nov. 1984.

Hebert, T. & Leahy, R. (1989). A generalized EM algorithm for 3-D Bayesian reconstruction from Poisson data using Gibbs priors, *IEEE Transactions on Medical Imaging*, vol. 8, no. 12, pp. 194 – 202, 1989.

Jackson, D.; Iborra, F.; Manders, E. & Cook P. (1998). Numbers and organization of RNA polymerases, nascent transcripts, and transcription units in HeLa nuclei. *Mol. Biol. Cell*, vol. 9, pp. 1523–1536, 1998.

Kervrann, C. & Trubuil, A. (2004). An adaptive window approach for Poisson noise reduction and structure preserving in confocal microscopy, *International Symposium on Biomedical Imaging, ISBI'04*, Arlington, VA, April 2004.

Lichtman, J. W. & Conchello, J. A. (2005). Fluorescence microscopy. *Nat Methods*, vol. 2, no. 12, pp. 910–9, 2005.

Lippincott-Schwartz, J.;Altan-Bonnet, N. & Patterson, G. H. (2003). Photobleaching and photoactivation: following protein dynamics in living cells. *Nat Cell Biol*, vol. Suppl,S7-14 September 2003. [Online]. Available: http://view.ncbi.nlm.nih.gov/pubmed/14562845.

Lippincott-Schwartz, J.; Snapp, E. & Kenworthy, A. (2001). Studying protein dynamics in living cells. *Nat Rev Mol Cell Biol*. 2:444-56.

Moon, T. K. & Stirling, W. C. (2000). *Mathematical methods and algorithms for signal processing*. Prentice-Hall.

Rudin, S. L. & Fatemi, E. (1992). Nonlinear total variation based noise removal algorithms, *Physica D*, vol. 60, pp. 259–268, 1992.

Timmermann, K.E. & Nowak, R.D.(1999). Multiscale modeling and estimation of Poisson processes with application to photon-limited imaging, *IEEE Transactions on Information Theory*, vol. 45, no. 3, pp. 846–862, Apr 1999.

Underwood, R. (2007). Frap and flip, photobleaching technique to reveal cell dynamics, 2007. [Online]. Available: http://www.nikoninstruments.com/images/stories/litpdfs/nikon_note_3nn06_8_07_lr.pdf.

Vogel, C. & Oman, M. (1998). Fast, robust total variation-based reconstruction of noisy, blurred images, 1998. [Online]. Available: citeseer.ist.psu.edu/vogel98fast.html.

Willett, R. (2006). "Statistical analysis of photon-limited astronomical signals and images, *Statistical Challenges in Modern Astronomy IV (SCMA IV)*, 2006. [Online]. Available: http://www.ee.duke.edu/ willett/papers/WillettSCMA2006.pdf.

Willett, R.M. & Nowak, R.D. (2004). Fast multiresolution photon-limited image reconstruction, *IEEE International Symposium on Biomedical Imaging: Nano to Macro, 2004.*, pp. 1192–1195 Vol. 2, 15-18 April 2004.

Wohlberg, B. & Rodríguez, P. (2007). An iteratively reweighted norm algorithm for minimization of total variation functionals, *IEEE Signal Processing Letters*, vol. 14, no. 12, pp. 948 – 951, 2007.


**Recent Advances in Biomedical Engineering**

Edited by Ganesh R Naik

ISBN 978-953-307-004-9
Hard cover, 660 pages
**Publisher** InTech
**Published online** 01, October, 2009
**Published in print edition** October, 2009

The field of biomedical engineering has expanded markedly in the past ten years. This growth is supported by advances in biological science, which have created new opportunities for development of tools for diagnosis and therapy for human disease. The discipline focuses both on development of new biomaterials, analytical methodologies and on the application of concepts drawn from engineering, computing, mathematics, chemical and physical sciences to advance biomedical knowledge while improving the effectiveness and delivery of clinical medicine. Biomedical engineering now encompasses a range of fields of specialization including bioinstrumentation, bioimaging, biomechanics, biomaterials, and biomolecular engineering. Biomedical engineering covers recent advances in the growing field of biomedical technology, instrumentation, and administration. Contributions focus on theoretical and practical problems associated with the development of medical technology; the introduction of new engineering methods into public health; hospitals and patient care; the improvement of diagnosis and therapy; and biomedical information storage and retrieval. The book is directed at engineering students in their final year of undergraduate studies or in their graduate studies. Most undergraduate students majoring in biomedical engineering are faced with a decision, early in their program of study, regarding the field in which they would like to specialize. Each chosen specialty has a specific set of course requirements and is supplemented by wise selection of elective and supporting coursework. Also, many young students of biomedical engineering use independent research projects as a source of inspiration and preparation but have difficulty identifying research areas that are right for them. Therefore, a second goal of this book is to link knowledge of basic science and engineering to fields of specialization and current research. The editor would like to thank the authors, who have committed so much effort to the publication of this work.

**How to reference**

In order to correctly reference this scholarly work, feel free to copy and paste the following:

Isabel Rodrigues and Joao Sanches (2009). Denoising of Fluorescence Confocal Microscopy Images with Photobleaching compensation in a Bayesian framework, Recent Advances in Biomedical Engineering, Ganesh R Naik (Ed.), ISBN: 978-953-307-004-9, InTech, Available from: http://www.intechopen.com/books/recent-advances-in-biomedical-engineering/denoising-of-fluorescence-confocal-microscopy-images-with-photobleaching-compensation-in-a-bayesian-

INTECH
open science | open minds

**InTech Europe**
University Campus STeP Ri

**InTech China**
Unit 405, Office Block, Hotel Equatorial Shanghai

www.intechopen.com

Slavka Krautzeka 83/A
51000 Rijeka, Croatia
Phone: +385 (51) 770 447
Fax: +385 (51) 686 166
www.intechopen.com

No.65, Yan An Road (West), Shanghai, 200040, China
中国上海市延安西路65号上海国际贵都大饭店办公楼405单元
Phone: +86-21-62489820
Fax: +86-21-62489821